Chapter 5
Control Goals

C. Westermayer and A. Schirrer

5.1 Analysis of Aircraft Dynamics

C. Westermayer and A. Schirrer

This section summarizes the open-loop dynamic behavior of the considered ACFA BWB aircraft predesign model as relevant for control design, both for longitudinal and lateral dynamics. The longitudinal analysis itself is based on the ROM from Chap. 4, has been developed in [13] and is summarized in the following from there. It starts with analyzing the system eigendynamics, where it is shown that longitudinal static stability does not exist over the entire parameter range. An investigation of the system response to control and disturbance inputs in both time-domain and frequency-domain exposes the constrained applicability of available control surfaces. Additionally, the effect of turbulence gusts on the system structural dynamics is shown and maximum load levels are determined. Based on a sensitivity analysis, the system dependency on flight parameters and fuel mass is evaluated, which provides essential insight for parameter dependent and robust control design. The influence of conventional feedback loops on the system dynamics is outlined using relevant root locus plots. A shortened lateral analysis taken from [10] follows in an analogous fashion.

5.1.1 Overview on the System Models for Control Design and Validation

Dynamic predesign models of the ACFA BWB 450-passenger aircraft configuration have been developed during the ACFA 2020 research project as described in Part 1

C. Westermayer · A. Schirrer (✉)
Vienna University of Technology, Vienna, Austria
e-mail: alexander.schirrer@tuwien.ac.at

M. Kozek and A. Schirrer (eds.), *Modeling and Control for a Blended Wing Body Aircraft*,
Advances in Industrial Control, DOI 10.1007/978-3-319-10792-9_5

of this book [12]. These integrated models represent the longitudinal as well as the lateral flight mechanics of the RB aircraft motion, the flexible structure mechanics, as well as the aeroelastic coupling of the RB and the flexible dynamics. The finite element method (FEM) has been utilized for structural design; panel- and computational fluid dynamics (CFD) methods have been applied to obtain aerodynamic data. Compared to earlier studies (see [6–9, 14]) based on the large 750-passenger NACRE BWB configuration (see Sect. 3.2 and [2]), the present models consider a redesigned, downsized BWB configuration.

Four relevant parameters are considered of having a major effect on the dynamic system behavior: the flight parameters *airspeed* and *dynamic pressure* as well as the two structure parameters *fuel-filling level* and *center of gravity (CG) position*. The longitudinal and lateral flight mechanics equations have been linearized about level trimmed flight conditions at fixed parameter gridpoints, and the flexible structure modes have been modeled and separated into symmetric and antisymmetric modes. Then, due to the symmetry of the aircraft configuration, the lateral dynamics is decoupled from the longitudinal dynamics for small perturbations of the flight mechanic variables (in particular, for sufficiently small perturbations of sideslip, roll, and yaw angles). In this predesign stage, no further quantification of lateral–longitudinal coupling effects has been done because the main objectives of the conducted studies target control design and loads alleviation in trimmed level flight conditions or in typical, moderate turn maneuvers.

5.1.2 Models of Longitudinal Dynamics

The longitudinal input/output (I/O) configuration of the BWB aircraft is depicted in Fig. 5.1.

The reduced longitudinal models $\boldsymbol{G}$ are given in state-space representation

$$\begin{bmatrix} \dot{\mathbf{x}}(t) \\ \mathbf{e}(t) \\ \mathbf{y}(t) \end{bmatrix} = \underbrace{\begin{bmatrix} \mathbf{A} & \mathbf{B}_1 & \mathbf{B}_2 \\ \mathbf{C}_1 & \mathbf{D}_{11} & \mathbf{D}_{12} \\ \mathbf{C}_2 & \mathbf{D}_{21} & \mathbf{D}_{22} \end{bmatrix}}_{\boldsymbol{G}_{\mathrm{ac}}} \begin{bmatrix} \mathbf{x}(t) \\ \mathbf{d}(t) \\ \mathbf{u}(t) \end{bmatrix} \tag{5.1}$$

with the corresponding state vector

$$\mathbf{x} = \left[X \; u \; Z \; w \; \Theta \; q \; \xi_1 \; \dot{\xi}_1 \; \ldots \; \xi_s \; \dot{\xi}_s \; x_{l_1} \; \ldots \; x_{l_t} \right]^{\mathrm{T}}, \tag{5.2}$$

where the first six states represent the RB states x-position X, body forward velocity u, z-position Z, body downward velocity w, pitch angle Θ and pitch rate q, respectively. If the integrator states X and Z are not considered, they are removed by truncation. The number of remaining rigid body (RB) states is then $r = 4$. The states ξ_j and $\dot{\xi}_j$ $(j = 1, \ldots, s)$ are the modal deflections and modal deflection rates of

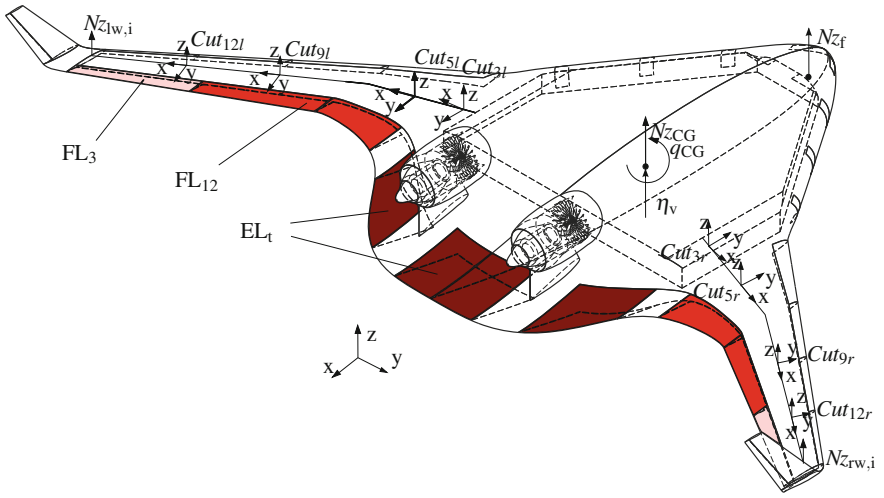

Fig. 5.1 Schematic sketch of BWB aircraft with relevant system inputs and outputs [13]

aeroelastic modes, respectively, and x_{l_k} $(k = 1, \ldots, t)$ are the lag states. The number of flexible modes and lag states are different for validation and design model, leading to the total numbers of states $n_{x,i}$:

- Validation model $\mathbf{G}_{\text{ac,val}}$: $r = 4, s = 19, t = 14 \Rightarrow \quad n_{x,\text{val}} = 62$
- Design model $\mathbf{G}_{\text{ac,des}}$: $r = 4, s = 2, t = 4 \quad \Rightarrow \quad n_{x,\text{des}} = 12$

The number of flexible modes is set to a comparatively low number due to the limited bandwidth of about 20 rad/s of the investigated control surfaces. However, within this range, the first two symmetrical flexible modes are located which are important in terms of structural loads and vibrations as will be shown in the open-loop system analysis in Sect. 5.1.3. Moreover, keeping only four lag states in the design model turned out to have only marginal effect on the considered system dynamics.

In general, it is reasonable to keep the system order of the aeroelastic design model as low as possible mainly for two reasons:

1. The controller order depends on the design system order when using $\mathscr{H}_\infty$-based design methodologies.
2. The system order strongly influences computational cost and conservativeness in control design.

The BWB aircraft is equipped with five flaps distributed along the trailing edge of the center body and the wing, all available for longitudinal control. Early investigations have shown that in order to obtain sufficient control authority for pitch control, all four flaps at the center body have to be used, forming together the combined elevator EL_t. Although the combined inner two flaps at the wing FL_{12} are mainly dedicated for lateral control [10], they also play an important role for longitudinal maneuver

load control. The outer flap at the wing FL_3 will be mainly used for aeroelastic control. The two engines of the aircraft are mounted at the rear, above the center body, and produce the symmetric thrust T_{12}. The control input vector of the system $\mathbf{u}$ is thus given by:

$$\mathbf{u} = \left[\delta_{\mathrm{EL}_t} \ \dot{\delta}_{\mathrm{EL}_t} \ \delta_{\mathrm{FL}_{12}} \ \dot{\delta}_{\mathrm{FL}_{12}} \ \delta_{\mathrm{FL}_3} \ \dot{\delta}_{\mathrm{FL}_3} \ T_{12} \right]^{\mathrm{T}}, \tag{5.3}$$

where δ_i and $\dot{\delta}_i$ is the symmetric deflection and deflection rate of the respective control surface. Besides these control inputs, the aircraft model is equipped with various exogenous inputs $\mathbf{d}$:

$$\mathbf{d} = \left[\eta_{\mathrm{v}} \ \eta_{\mathrm{2D},1} \ \dot{\eta}_{\mathrm{2D},1} \ \ldots \ \eta_{\mathrm{2D},33} \ \dot{\eta}_{\mathrm{2D},33} \right]^{\mathrm{T}}. \tag{5.4}$$

A global vertical gust velocity input η_{v} positioned at the CG is most relevant for the given study. Moreover, the model has zonal vertical gust velocity $\eta_{\mathrm{2D},i}$ and acceleration $\dot{\eta}_{\mathrm{2D},i}$ inputs distributed along the structure which can be fed by a 2D von-Kármán turbulence spectrum [4, 5].

The system model comprises 511 outputs which are basically divided into two groups: measurements $\mathbf{y}$ and exogenous outputs $\mathbf{e}$. Measurements utilized in this work are:

$$\mathbf{y} = \left[Nz_{\mathrm{CG}} \ q_{\mathrm{CG}} \ V_{\mathrm{TAS}} \ \Theta_{\mathrm{CG}} \ \alpha_{\mathrm{CG}} \ Nz_{\mathrm{f}} \ Nz_{\mathrm{rw},i} \ Nz_{\mathrm{lw},i} \ Nz_{\mathrm{long.law}} \right]^{\mathrm{T}}, \tag{5.5}$$

where Nz_{CG}, q_{CG}, Θ_{CG} and α_{CG} are the vertical acceleration, pitch rate, pitch angle and the angle of attack at the CG position, respectively, V_{TAS} is the true airspeed, Nz_{f} is the vertical acceleration at the front position (cockpit position) and $Nz_{\mathrm{rw},i}$, $Nz_{\mathrm{lw},i}$ are several vertical acceleration outputs distributed over the wing. The $Nz_{\mathrm{long.law}}$ output is a longitudinal modal wing bending acceleration signal used to separate the symmetric vertical wing bending from the RB motion

$$Nz_{\mathrm{long.law}} = \left(\frac{\left(Nz_{\mathrm{lw},k} + Nz_{\mathrm{rw},k} \right)}{2} - Nz_{\mathrm{CG}} \right), \tag{5.6}$$

where the index k refers to a selected pair of sensors obtained using a sensor placement optimization technique [3]. The exogenous output vector is given as follows:

$$\mathbf{e} = \left[My_1 \ \ldots \ My_{14} \ Fz_1 \ \ldots \ Fz_{14} \right]^{\mathrm{T}}, \tag{5.7}$$

where My_i represent the cut bending moments and Fz_i the cut vertical forces equally distributed along the wing as exemplarily shown in Fig. 5.1. From this set of structural load outputs, a subset is selected for controller design in order to formulate performance specifications concerning load minimization in turbulence gust and maneuvers. In the validation model, the entire set is utilized to evaluate closed-loop performance.

Table 5.1 Dynamical properties of control surface actuators for $\theta_q = 17{,}238$ and corresponding deflection and rate limits

	Frequency in rad/s	Relative damping (−)	Deflection limit in deg	Rate limit in deg/s
EL_t	2.72	0.71	$-30 \leq \eta_{EL_t} \leq 15$	$-30 \leq \dot{\eta}_{EL_t} \leq 30$
FL_{12}	4.44	0.71	$-25 \leq \eta_{FL_{12}} \leq 25$	$-40 \leq \dot{\eta}_{FL_{12}} \leq 40$
FL_3	7.80	0.71	$-25 \leq \eta_{FL_3} \leq 25$	$-40 \leq \dot{\eta}_{FL_3} \leq 40$

The aircraft model $\mathbf{G}_{\text{ac}}$ according to (5.1)–(5.7) has to be augmented with corresponding linear actuator $\mathbf{G}_{\text{act}}$ and sensor dynamics $\mathbf{G}_{\text{sen}}$ in order to finally obtain the model for controller design and validation:

$$\mathbf{G} = \mathbf{G}_{\text{act}}\, \mathbf{G}_{\text{ac}}\, \mathbf{G}_{\text{sen}}. \tag{5.8}$$

The dynamical properties of the linearized second-order control surface actuator models for the maximum dynamical pressure and the corresponding deflection and rate limits are provided in Table 5.1. The actuator matrix $\mathbf{G}_{\text{act}}$ therefore can be written as

$$\mathbf{G}_{\text{act}} = \begin{bmatrix} \frac{7.5}{s^2+3.9s+7.5} & 0 & 0 & 0 & 0 \\ \frac{7.5s}{s^2+3.9s+7.5} & 0 & 0 & 0 & 0 \\ 0 & \frac{19.7}{s^2+6.3s+19.7} & 0 & 0 & 0 \\ 0 & \frac{19.7s}{s^2+6.3s+19.7} & 0 & 0 & 0 \\ 0 & 0 & \frac{60.7s}{s^2+11.0s+60.7} & 0 & 0 \\ 0 & 0 & \frac{60.7s}{s^2+11.0s+60.7} & 0 & 0 \\ 0 & 0 & 0 & \frac{152e3}{5.8s+1} & 0 \\ 0 & 0 & 0 & 0 & \mathbf{I}_{\text{d}} \end{bmatrix}, \tag{5.9}$$

with $\mathbf{I}_{\text{d}}^{m\times m}$ as the identity matrix of appropriate dimensions according to the number of disturbance inputs m. As a result of the system extension by actuator dynamics, the input vector (5.3) is replaced by:

$$\mathbf{u} = \begin{bmatrix} \eta_{EL_t} & \eta_{FL_{12}} & \eta_{FL_3} & \eta_{T_{12}} \end{bmatrix}^{\text{T}}, \tag{5.10}$$

where η_{surf} are the respective symmetric control surface deflection and thrust inputs. The sensor delays are defined as 2nd-order Padé approximations, whereas for safety critical measurements, such as $\mathbf{y}(1, \ldots, 6)$ from (5.5), the delay is set to 160 ms and for measurements utilized for aeroelastic control $\mathbf{y}(7, \ldots, 9)$, a delay of 60 ms is

assumed. Moreover, measurements $\mathbf{y}(1, \ldots, 6)$ are filtered by low-pass Butterworth filters given by the transfer function

$$\mathbf{G}_{\mathrm{BW}} = \frac{1}{0.00281s^2 + 0.075s + 1}. \tag{5.11}$$

In case of the design models, sensor delays and Butterworth filters are further approximated with only 1st-order Padé approximations and PT1 elements, leading to

$$\mathbf{G}_{\mathrm{sc}} = \frac{-15(s - 12.5)}{(s + 15)(s + 12.5)} \tag{5.12}$$

for safety critical measurements and to

$$\mathbf{G}_{\mathrm{ae}} = \frac{-(s - 33.3)}{(s + 33.3)} \tag{5.13}$$

for aeroelastic measurements. The sensor transfer function matrix is therefore given by:

$$\mathbf{G}_{\mathrm{sen}} = \mathrm{diag}\{\, \mathbf{G}_{\mathrm{sc}}\mathbf{I}^{r\times r}\ \mathbf{G}_{\mathrm{ae}}\mathbf{I}^{s\times s}\ \mathbf{I}^{t\times t}\,\}, \tag{5.14}$$

where r and s are the numbers of safety critical and aeroelastic measurements, respectively, and t the number of load outputs.

5.1.3 Open-Loop Analysis of Longitudinal Dynamics

5.1.3.1 System Eigendynamics

The longitudinal RB motion of the BWB aircraft is characterized by the short-period mode (SPM) and the phugoid mode (PM). Moreover, in the low-frequency region up to 3 rad/s the slowest lag state (LAG) and actuator mode actuator mode (AM) of the combined elevator EL_t appear. Depending on the considered parameter case, basically three different constellations of SPM and PM appear. Those are presented in Fig. 5.2, where in the left plot the full RB dynamics, that is, SPM and PM, are presented while in the right plot the corresponding SPM approximation due to omitted states u and Θ is shown.

1. The SPM forms a conjugate complex pole pair and the PM is given by two real poles, whereby one of them is unstable.
2. The SPM is given by two real stable poles while one phugoid pole is again stable and one is unstable.

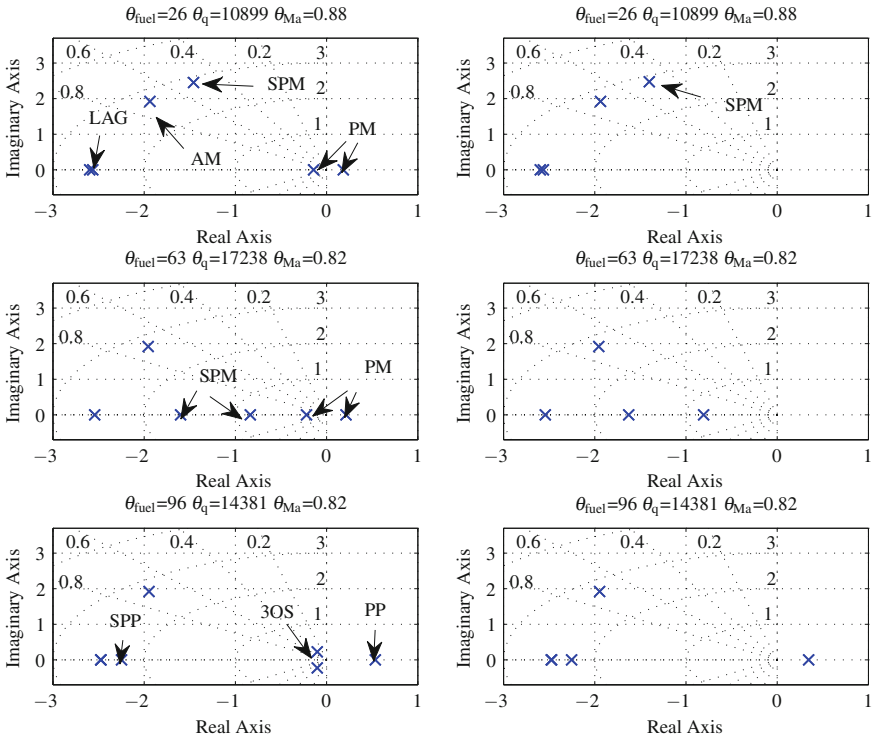

Fig. 5.2 Pole map of low-frequency poles for various parameter cases: model with RB states u, w, Θ, q (*left*) and with RB states w, q (*right*)

3. SPM and PM merge forming a so-called 3rd oscillation (3OS). The remaining two poles are real. One of them is faster and stable (SPP) and the other one is unstable (PP).

This development of pole constellations from 1 to 3 is attained with parameter settings toward higher fuel mass θ_{fuel}, increased dynamic pressure θ_q and lower Mach numbers θ_{Ma}. The EL_t actuator mode AM is hardly changed for varying pressure parameters θ_q, however, it is located rather close to the SPM. This can lead to undesirable interaction of those two modes due to feedback control.

In the first two cases, a similar position for the SPM is visible. In the third case, the SPM is given by two real poles, where one of them is stable and one unstable. Therefore, for parameter settings corresponding to the third case, the system dynamics is characterized by a fast and unstable SPM, which in turn indicates longitudinal static instability of the aircraft.

The pole distribution of the flexible modes is shown in Fig. 5.3 for the whole parameter envelope.

The design model contains only two flexible modes, the first and second wing bending mode WB_1 and WB_2, respectively. Considering Fig. 5.3, it can be seen that

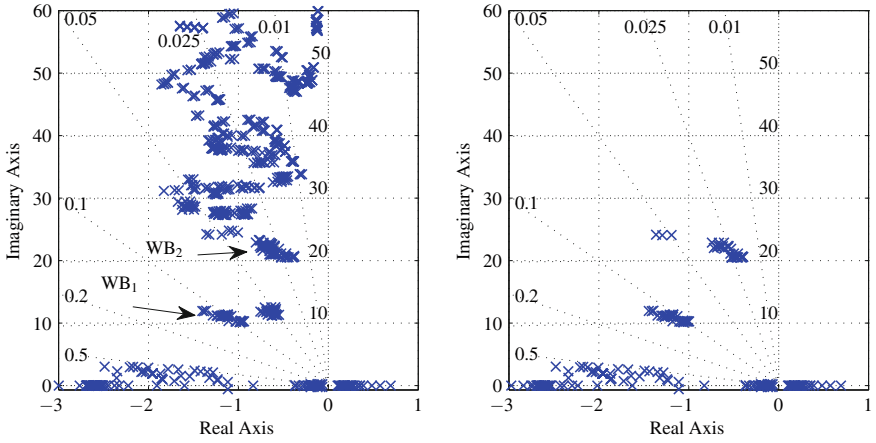

Fig. 5.3 Flexible mode pole distribution for entire envelope: validation model (*left*) and design model (*right*)

for both models WB_1 and WB_2 come to lie at similar positions which is an important requirement for control design. The remaining flexible modes in the validation model are located between 10 and 60 rad/s. However, these modes' frequencies are significantly above the actual bandwidth of the actuators and therefore out of scope of this study.

5.1.3.2 Input Response

Time-Domain Response

The following time-domain analysis provides a representative overview on system characteristics for both control surface inputs as well as disturbance inputs.

Control surface inputs: In Fig. 5.4 the unit step response from the control surfaces η_{EL_t}, $\eta_{FL_{12}}$ and η_{FL_3} to the flight mechanic outputs $Nz_{\text{long.law}}$, q_{CG} and to My_5 are shown. Note that the time responses drift away as a result of the unstable phugoid mode. The $Nz_{\text{long.law}}$ output extracts clearly the wing oscillations. In the lower plot, the structural load output My_5 is shown where high loads given by the pitch-down maneuver are notable. The general qualitative statements on system response hold for the entire parameter range despite the presence of strong variations in system dynamics.

Turbulence gust inputs: For evaluation of the system response in terms of the maximum arising structural loads and vibrations caused by turbulence, a standardized disturbance velocity signal given by the one-minus-cosine $(1-\cos)$ gust will be utilized throughout this work. This signal basically depends on two parameters, the integral scale length L_{gust} and the maximum vertical gust velocity

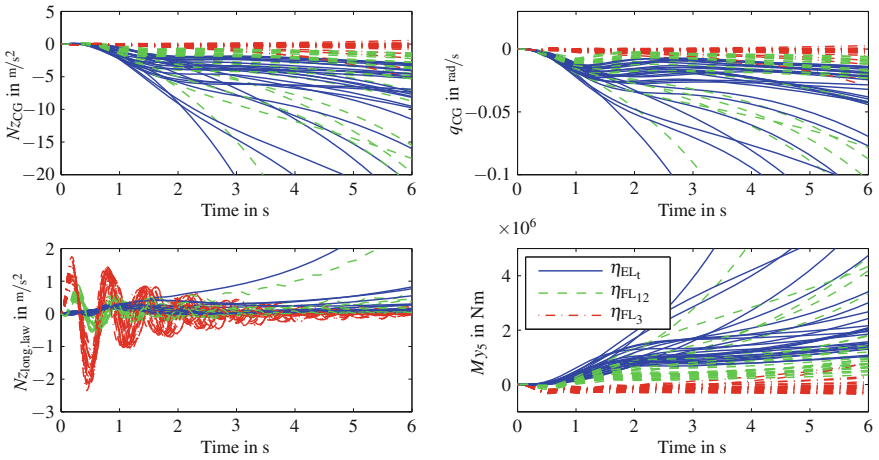

Fig. 5.4 Time response of selected relevant outputs to unit step inputs on combined elevator η_{EL_t}, combined inner flap $\eta_{FL_{12}}$ and outer flap η_{FL_3} for a representative set of parameter cases

$v_{z,\max} = v_{z,\max}(\theta_{Ma}, q)$. Shorter gusts excite mainly the flexible structure modes, while long gusts lead to excitation of the RB dynamics. It is noticeable that the gust of highest length corresponding to excitation in the low-frequency region leads to maximum acceleration and pitch rate values. Depending on the parameter case, maximum accelerations of 20 m/s^2 and above can occur. Similar to the flight mechanic outputs, also structural loads are maximal for long gusts. Shorter gusts, on the contrary, strongly excite flexible modes, resulting in long-lasting, weakly damped vibrations. Considering the $Nz_{long.law}$ output, for example, it turns out that a gust with length $L_{gust} = 30.5$ m causes the maximum wing bending acceleration. It is important to determine the parameter combination for aircraft and gust leading to maximum dynamical structural loads. The cut forces Fz_i and moments My_i at three different positions along the wing are evaluated. It turns out that the maximum structural loads at cut positions closer to the center are typically caused by the longest gusts. At outside cut positions, shorter gusts are more relevant.

Frequency-Domain Response

Considering the Nz_{CG} and q_{CG} responses, it turns out that the responses for the η_{EL_t} and $\eta_{FL_{12}}$ inputs is dominated by the low-frequency short-period mode. For pitch maneuver control, it is important that the elevator hardly excites the flexible modes. This also becomes evident when considering the responses for $Nz_{long.law}$ and My_5. The outer flap FL_3 shows highest magnitude at the frequency of the first wing bending mode WB_1. The controllability of the second wing bending mode WB_2 is low for this flap. FL_{12} appears to be an effective control input for both, flight mechanics and aeroelastics control.

The response for varying parameter cases from vertical gust input η_v to Nz_{CG} shows a flat characteristics until about 10 rad/s, while above it is dominated by the weakly damped WB_2 and a higher frequency flexible mode at around 50 rad/s. The $Nz_{long.law}$ response shows high-pass behavior, dominated by WB_1, WB_2, and again the flexible mode at 50 rad/s. For inside cut positions the cut load outputs Fz_i and My_i show high gain in the low-frequency region. The maximum magnitude is present at WB_2. Load outputs further outside show high-pass behavior, dominated by WB_1, WB_2, and modes at higher frequencies.

Root Locus of Relevant Feedback Loops

Before starting a multiobjective multi-input multi-output (MIMO) controller design, it is of utmost importance to understand the effects of single-input single-output (SISO) feedback loops. Effective loops for modification of the short-period mode and the phugoid mode are shown, and present limitations due to the slow actuator dynamics and sensor delays are outlined. The basic characteristics described in the following also hold for the remaining parameter cases.

In Fig. 5.5, the root locus for positive static feedback from q_{CG}, Nz_{CG} and Θ_{CG} on η_{EL_t} and negative static feedback from V_{TAS} on η_{EL_t} are shown. As can be seen from the top left plot, a q_{CG} feedback on EL_t significantly increases SPM damping.

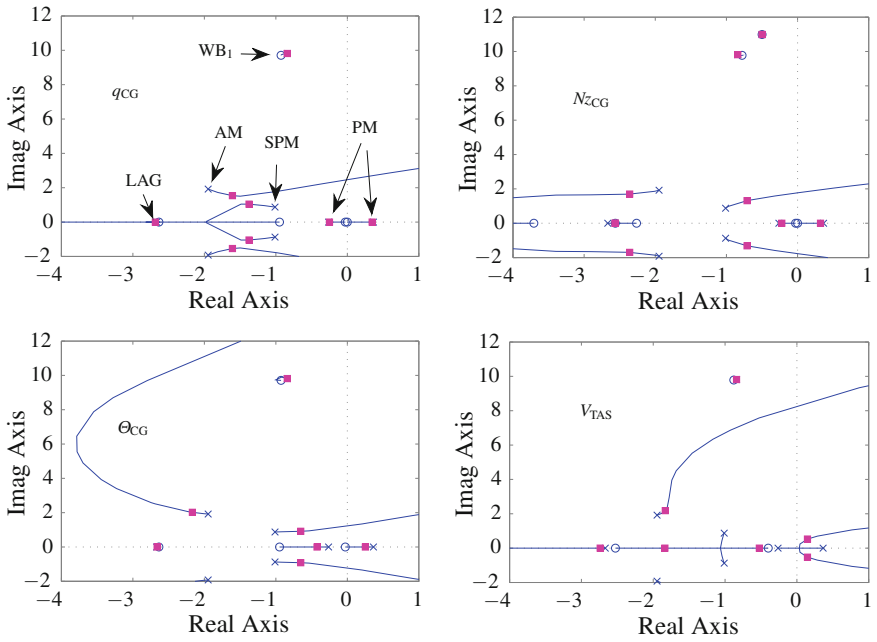

Fig. 5.5 Low-frequency root locus plots for $+q_{CG}$, $+Nz_{CG}$, $+\Theta_{CG}$ and $-V_{TAS}$ static feedback on η_{EL_t} for modification of SPM and PM

Likewise, the damping of the actuator mode is reduced to a similar extent. The location of the PM and the WB_1 is hardly changed. The latter also holds for Nz_{CG} feedback. Notably, this measurement has a destabilizing effect on the SPM, while the frequency is only slightly increased. A similar behavior can be detected for a Θ_{CG} feedback, with the exception that this output also slightly modifies the PM. The PM can be even more shifted by a negative feedback of V_{TAS} on η_{EL_t}. For the optimum static feedback gain, both poles are real and close to the imaginary axis. The SPM, on the contrary, forms two real poles, where one of them becomes significantly slower with increased feedback gain. Finally, the slowest lag state (LAG) is marginally modified due to the presented feedback loops.

The effectiveness of the wing trailing-edge control surfaces FL_{12} and FL_3 concerning flexible mode damping is evaluated using the modal wing bending acceleration signal $Nz_{long.law}$. The damping of the flexible mode WB_1 can be increased due to static feedback solely by the outer flap FL_3. Limitations due to the 60 ms delay become clearly evident: In the case of WB_2, the root locus even changes its direction when including the sensor delay. However, the actual pole shifting of WB_2 is rather moderate. This is different for feedback on FL_{12}, where the root locus for WB_2 is almost horizontal. Nevertheless, an increase of damping using static feedback is related to reduced damping of WB_1.

5.1.3.3 Sensitivity Analysis

The main results of the sensitivity analysis are summarized in the following from [13]. Evaluating the ν-gap metric as a control-oriented measure of plant variation for different parameter points θ_{Ma} and v for the range of fuel-mass parameters (potentially unknown to the controller), it can be seen that high values of the metric arise for flight parameter $\theta_{Ma} = 0.85$ which suggests this to be the most difficult θ_{Ma} parameter for obtaining robustness against uncertain fuel mass. Conversely, no strong correlation to the θ_q parameter is evident. For the considered flight control architectures, the flight parameters θ_{Ma} and θ_q are potential scheduling parameters for the BWB aircraft.

It can be concluded that an increased θ_{Ma} parameter is characterized by a faster SPM of reduced damping. Moreover, it turns out that the DC gain changes nonlinearly with the θ_{Ma} parameter and the maximum gain occurs for the low θ_{Ma} number case. For both parameters, ω and ζ, in general a linear dependency appears, however, with varying slope for different θ_q and θ_{fuel} parameters. Noticeable is specifically the different characteristic of the magnitude plot for same θ_{fuel} parameter but changing θ_{Ma} parameter. Generally, with increasing θ_q parameter, the frequency and the damping of the SPM is moderately increased. It can be concluded that the SPM pole location depends approximately linearly on flight parameters θ_q and θ_{Ma}, while the system input–output behavior deviates, partly significantly, from linear behavior.

5.1.4 Models of Lateral Dynamics

The lateral dynamics model is comprised of lateral flight mechanic states, antisymmetric flexible structure dynamic states, as well as lag states. The corresponding dynamic models are utilized to design and validate the lateral control laws in Chaps. 6 and 7 at various flight cases (defined by the parameters airspeed and dynamic pressure) and mass cases (defined by the parameters fuel-filling level and CG position).

Some comprehensive studies (for example, sizing loads alleviation performance, see Chap. 8) have been carried out for a total of several hundred aircraft parameter cases within a defined grid for these four parameters.

Many detail studies have been carried out at a selected flight case corresponding to cruise conditions. Then, a set of $k = 30$ linearized state-space systems $\mathbf{P}_i$, $i = 1, \ldots, k$ for various parameter values of fuel-filling level and CG position is studied:

$$\dot{\mathbf{x}} = \mathbf{A}_i \mathbf{x} + \mathbf{B}_i \mathbf{u} \tag{5.15}$$

$$\mathbf{y} = \mathbf{C}_i \mathbf{x} + \mathbf{D}_i \mathbf{u}. \tag{5.16}$$

The lateral state vector $\mathbf{x}$ is composed of 4 flight mechanic states (sideslip angle β, roll rate p, yaw rate r, roll angle ϕ), 12 elastic states (6 structural antisymmetric modes), as well as 7 lag states. The integrator states ψ (yaw angle) and y (horizontal displacement) are neglected in this study. These systems are augmented by actuator and sensor dynamics.

Utilized inputs $\mathbf{u}$ for control design are:

1. Symmetric rudder deflection and rate u_{RU}, $\dot{u}_{\mathrm{RU}}$
2. Combined antisymmetric trailing-edge control surface deflections and rates:
   a. u_{TE12}, $\dot{u}_{\mathrm{TE12}}$: middle and inner elevons (deflected equally)
   b. u_{TE3}, $\dot{u}_{\mathrm{TE3}}$: outer elevon

The actuator dynamics $\mathbf{G}_{\mathrm{act}}$ are modeled via 2nd-order low-pass filters as a low-order approximation of physically modeled control surfaces and actuation system dynamics. These models provide both the actual surface deflections as well as their rates as outputs $\left([u_j, \dot{u}_j]^{\mathrm{T}} = \mathbf{G}_{\mathrm{act},j}\, u_{\mathrm{command},j}\right)$.

Utilized outputs $\mathbf{y}$ for control design are:

1. Sideslip angle β
2. Roll angle ϕ
3. Roll rate p
4. Yaw rate r
5. Antisymmetric wingtip acceleration signal $Nz_{\mathrm{lat.law}} = Nz_{\mathrm{r.wingtip}} - Nz_{\mathrm{l.wingtip}}$ where $Nz_{\mathrm{r.wingtip}}$ and $Nz_{\mathrm{l.wingtip}}$ are vertical accelerations at the right and left wingtips, respectively,

which are each considered subject to time delays due to signal processing latencies (160 ms for outputs (1–4), 60 ms for output (5)), modeled via 2nd-order Padé

Table 5.2 System modes of the lateral open-loop dynamics

Aircraft system mode	Pole characteristics	Frequency (rad/s)
DR mode	Oscillatory, low-damped/unstable	1
Roll resilience mode	Real, stable	2...3
Spiral mode	Real, slow, unstable	0.001
1st anti-sym. flexible mode	Oscillatory, low-damped	10
2nd anti-sym. flexible mode	Oscillatory, low-damped	20

approximations. Additionally 2nd-order low-pass Butterworth filters are applied to outputs (1–4). Note that output (5) acts as an effective, simplified modal sensor for the antisymmetric flexible modes. It amplifies these modes' amplitudes, however, it is not compensated for the effect of roll rate change (RB motion) for simplicity. The sensor dynamics is collected into $\mathbf{G}_{\text{sens}}$, and the augmented system $\widetilde{\mathbf{P}}_i = \mathbf{G}_{\text{sens}}\mathbf{P}_i\mathbf{G}_{\text{act}}$ is of order 47.

Additional exogenous input and output signals are considered for system analysis and validation: a wind gust disturbance input is modeled by an aggregated lateral wind speed input signal

$$d = v_{\text{lat}}, \tag{5.17}$$

as well as a structure load output (a cut moment at the wing)

$$z = M y_{\text{wing}}. \tag{5.18}$$

5.1.5 Open-Loop Analysis of Lateral Dynamics

The open-loop system eigendynamic parameters can be seen in Table 5.2: A low-damped or unstable Dutch Roll mode (DR mode) and the two real flight mechanic modes (spiral, roll resilience) are present. The first two antisymmetric flexible modes are located around 10 and 20 rad/s, respectively. Table 5.3 lists the pole locations of the dominating PT2 behavior of the linearized actuator models for the actuators of

Table 5.3 Eigenfrequencies of the linearized actuator models

Linearized control surface mode (dominant 2nd-order dynamics)	Pole characteristics
Flaps 3, 4	Damping $\zeta = \sqrt{2}/2$ at $\omega_{\text{d}} = 4.4$ rad/s
Flaps 5	Damping $\zeta = \sqrt{2}/2$ at $\omega_{\text{d}} = 7.8$ rad/s
Rudder	Damping $\zeta = \sqrt{2}/2$ at $\omega_{\text{d}} = 10.3$ rad/s

flaps 3, 4, 5, and the rudder. As seen from these numbers, the control design task is expected to be challenging for flexible modes control because these are located at or above the actuators' bandwidth. Open-loop responses for the lateral dynamics are given in the lateral control design sections (Sects. 6.2, 6.3, and 7.2).

5.2 Control Goals

A. Schirrer and C. Westermayer

This section lists the primary control goals formulated for the ACFA BWB aircraft predesign model both for the longitudinal and lateral dynamics. Subsets or specific variants of these goals are treated later in the respective control design sections of Chaps. 6 (feedback designs) and 7 (feed-forward designs).

5.2.1 Longitudinal Control Design Goals

The following general set of goals are addressed in the longitudinal control designs:

1. Stabilize the unstable short-period mode.
2. Slow down the unstable phugoid, such that the pole pair stays real and the maximum real part of the unstable pole p is limited by $\max(\mathrm{Re}(p)) < 0.1$.
3. Track the reference command input given by the vertical acceleration at the CG position Nz_{CG}. The rise time of Nz_{CG} to a unit step command input must be between 3 and 5 s and no overshoot is tolerated.
4. Overshoot of accompanying pitch rate response at the CG position, q_{CG}, must be lower than 30 %.
5. Reject disturbances from control inputs and external excitations within 5–7 s.
6. Unify the system dynamical behavior throughout the considered operating range in order to obtain similar closed-loop response.
7. Minimize maximum vertical accelerations of Nz_{CG} and Nz_{f} due to turbulence gust.
8. Constrain the demanded control signals by maximum deflection and deflection rate limits according to Table 5.1.
9. Investigate and demonstrate robustness against uncertainties of the fuel-mass parameter.
10. All control surfaces on the trailing edge can be utilized as actuators. However, the combined inner flap FL_{12} is also utilized for lateral control, consequently only restricted use for longitudinal control is possible.
11. Besides Nz_{CG} also q_{CG}, Nz_{f}, V_{TAS} and Θ_{CG} are available as flight mechanic measurements. Generally, the number of utilized measurement signals for the controller must be kept as low as possible.

Table 5.4 Control goals for the lateral control design tasks

General and tracking specifications	
DR mode	$\zeta_{DR} > 0.7$, ω_{DR} unchanged
Decoupling	Generate inputs with high coupling to roll and sideslip angles and low cross-coupling
Roll angle ϕ	DC gain similar for all mass cases, rise time to 90 % in $t_{rise} < 7$ s, max. 5 % overshoot
Sideslip angle β	DC gain similar for all mass cases, $t_{rise} < 5$ s
Robustness	Stable controller, Robust Stability (RS) and Robust Performance (RP) for all mass cases
Disturbance rejection specifications	
Minimize the influence of lateral gust on roll, sideslip, and lateral acceleration, while obeying the tracking specifications above. Moreover, the loads must not be increased	
Maneuver loads alleviation specifications	
Robustly minimize sizing *Fz*, *Mx*, and *My* loads along the wing in 60° roll maneuvers	

The requirements 1–7 are typical design goals of a so-called stability augmentation system (SAS) [1, 11] in order to align the closed-loop RB motion to pilot needs. Moreover, fulfilling these requirements provides an improved basis for subsequent autopilot design. Requirements 1, 2 and 6 are directly linked to closed-loop pole location and can therefore be addressed only by a feedback control approach, while requirements 3, 4 are also main goals of feed-forward design (see Chap. 7). Disturbance rejection (4) and acceleration minimization (7) based on a disturbance feed-forward concept is not investigated in this work. The limited actuator bandwidth (8) and the robustness requirements regarding fuel-mass uncertainty (9) are further essential aspects for an integrated flexible aircraft design which have to be considered at an early design phase.

5.2.2 Lateral Control Design Goals

The goals followed in lateral control design for the considered BWB aircraft are specified in Table 5.4.

References

1. Brockhaus R (2001) Flugregelung (English: Flight control). Springer, Berlin
2. European Commission (2014) Flying high with innovative aircraft concepts. http://ec.europa.eu/research/research-for-europe/transport-nacre_en.html
3. Hemedi M, Schirrer A, Westermayer C, Kozek M (2011) Integrated input-output selection strategy for robust control of complex parameter depending systems. J Syst Des Dyn (Special Issue of Motion and Vibration Control 2010) 5(5):1106–1118. Invited

4. Imbert N, Mouyon P, Montseny G (2000) State representation and simulation of 2nd turbulent wind. In: AIAA modelling and simulation technologies, Denver
5. Mouyon P, Imbert N (2002) Identification of a 2nd turbulent wind spectrum. Aerosp Sci Technol 6:599–605
6. Schirrer A, Westermayer C, Hemedi M, Kozek M (2010) LQ-based design of the inner loop lateral control for a large flexible BWB-type aircraft. In: 2010 IEEE multi-conference on systems and control, Yokohama, Japan
7. Schirrer A, Westermayer C, Hemedi M, Kozek M (2010) Robust control design parameter optimization via genetic algorithm for lateral control of a BWB type aircraft. In: IFAC workshop on intelligent control systems, Sinaia, Romania
8. Schirrer A, Westermayer C, Hemedi M, Kozek M (2011) Multi-model convex design of a scheduled lateral feedforward control law for a large flexible BWB aircraft. In: Preprints of the 18th IFAC world congress, Milano, Italy, pp 2126–2131
9. Schirrer A, Westermayer C, Hemedi M, Kozek M (2011) Robust convex lateral feedback control synthesis for a BWB aircraft. In: Preprints of the 18th IFAC world congress, Milano, Italy, pp 7262–7267
10. Schirrer A, Westermayer C, Hemedi M, Kozek M (2013) Robust lateral blended-wing-body aircraft feedback control design using a parameterized LFR model and DGK-iteration. In: Progress in flight dynamics, guidance, navigation, control, fault detection, and avionics, vol 6. EDP Sciences, pp 749–766
11. Stevens BL, Lewis FL (2003) Aircraft control and simulation. Wiley, New York
12. Stroscher F, Petersson Ö, Leitner M (2010) Aircraft structural optimization subject to flight loads—application to a wide body commercial aircraft configuration. In: EASN international workshop on aerostructures, Oct 2010
13. Westermayer C (2011) 2DOF parameter-dependent longitudinal control of a blended wing body flexible aircraft. PhD thesis, Vienna University of Technology
14. Westermayer C, Schirrer A, Hemedi M, Kozek M (2010) Linear parameter-varying control of a large blended wing body flexible aircraft. In: 18th IFAC symposium on automatic control in aerospace, Nara, Japan